RESEARCH ARTICLE

ADVANCED MATERIALS
www.advmat.de

High Efficiency and Stable Flexible Organic Solar Cells Facilitated by Light Sensitive Hydrophilic-to-Hydrophobic Converting Surface Modification of the Flexible Barrier Films

Yang Chen, Chao Yue, Wei Xiong, Yunfei Han, Hui Xu, Ke Shui, Shutao Yang, Jian Qin, Lianping Zhang, Zhiyun Li, Yabin Zhang, Wei-Shi Li, Chang-Qi Ma,* and Qun Luo**

With the advantages of high efficiency and flexibility, the flexible organic solar cells (FOSCs) showed great application in wearable electronics. However, degradation of device performance due to the infiltration of water and oxygen into the flexible substrate becomes the main obstacle to its development. The traditional encapsulation with a sandwich structure would reduce the optical and mechanical properties of the devices and increase the device's weight. In this work, a strategy of in situ fabrication of highly efficient and long-term stable FOSCs on the highly transparent barrier film (BF) substrates is developed. A kind of light-sensitive material, o-nitrobenzyl alcohol derivatives, which can convert from hydrophilic to hydrophobic, is induced to improve the wettability of AgNWs on the substrate and enable the printing fabrication of a uniform AgNWs transparent electrode. After light conversion, the NBE films are converted to hydrophobic, which sufficiently improved the barrier property. The efficiency of the BF/NBE devices reached 16.33% and retained 80% of its initial value after being stored in the air for 600 h, which is compared to the grid devices with the glass substrate. Besides, due to the superior mechanical properties and thin thickness, the in situ FOSCs with barrier substrates exhibited excellent mechanical bending durability.

1. Introduction

Flexible organic solar cells (FOSCs) have great potential in portable and wearable electronics due to their advantages of high efficiency,[1–3] flexibility,[4–11] light weight,[12–15] and compatibility with Roll-to-Roll processes.[16–18] At present, the power conversion efficiency (PCE) of FOSCs has developed quickly, with a maximum PCE of the small area device above 19%,[19] which is nearly satisfying the application requirement. However, the long-term stability of FOSCs remains a critical challenge for their large-scale commercialization.[20,21] Unlike the rigid devices with glass substrates, the FOSCs used plastic substrates.[22,23] The glass substrate is naturally an excellent water and oxygen barrier material,[24,25] while most of the plastic substrates, i.e., polyethylene terephthalate (PET), polyethylene naphthalate (PEN), polyimide (PI), etc., exhibit poor water prevention properties, which is the main reason for the poor stability of the FOSCs relative to the rigid devices.[26–29] Therefore, developing an advanced encapsulation strategy or substrate engineering approach to mitigate moisture is essential for realizing the commercial potential of FOSCs for practical applications. To improve the stability of flexible devices, several strategies, including encapsulation of the device through atomic layer deposition (ALD) or chemical vapor deposition (CVD), have been developed. For instance, Chen et al.[30] encapsulated the OSC devices with poly(divinylbenzene) (PDVB) film from the top of the devices through CVD. After encapsulation, the device efficiency showed less than 8% degradation. Similarly, Chang et al.[31] deposited Al_2O_3 film onto polyethylene terephthalate (PET) substrate as the encapsulation layer for glass devices.

Y. Chen, W. Xiong, Y. Han, H. Xu, K. Shui, S. Yang, J. Qin, L. Zhang, C.-Q. Ma, Q. Luo
i Lab & Printable Electronics Research Center
Suzhou Institute of Nano Tech and Nano Bionics
Chinese Academy of Sciences (CAS)
Suzhou 215123, P. R. China
E-mail: cqma2011@sinano.ac.cn; qluo2011@sinano.ac.cn

Y. Chen, C.-Q. Ma, Q. Luo
School of Nano-Tech and Nano-Bionics
University of Science and Technology of China
Hefei 230027, P. R. China

Z. Li, Y. Zhang
Vacuum Interconnected Nanotech Workstation
Suzhou Institute of Nano Tech and Nano Bionics
Chinese Academy of Sciences (CAS)
Suzhou 215123, P. R. China

C. Yue, W.-S. Li
Key Laboratory of Synthetic and Self-assembly Chemistry for Organic Functional Molecules
Center for Excellence in Molecular Synthesis
Shanghai Institute of Organic Chemistry
Chinese Academy of Sciences
Shanghai 200032, P. R. China
E-mail: liws@sioc.ac.cn

The ORCID identification number(s) for the author(s) of this article can be found under https://doi.org/10.1002/adma.202510780

DOI: 10.1002/adma.202510780

The encapsulation layer showed excellent moisture and oxygen barrier properties, with an oxygen transmission rate (OTR) of 1.9×10^{-3} cm^3 m^{-2} day^{-1} and a water vapor transmission rate (WVTR) of 9.0×10^{-4} g m^{-2} day^{-1}. Thanks to the good water barrier property of the Al_2O_3 encapsulation layer and the glass substrate, the devices showed negligible degradation after being exposed to the ambiance (30 °C, 65% relative humidity) for more than 40 days.[32] Another common strategy involves encapsulating the devices with flexible encapsulation barrier films via a sandwiched encapsulation structure.[33,34] For instance, Zheng et al.[35] utilized a surface-tethered nanostructured fluorinated molecular protection layer to encapsulate the stretchable polymer semiconductors. These fluorinated films exhibited enhanced resistance to degradation under the ambient environment and simultaneously served effectively against the absorption and diffusion of water or biofluids within the polymer substrate. With this method, surface-fluorinated devices sustained a high mobility of 1 cm^2 V^{-1} s^{-1} even after 56 days.

Although the sandwiched encapsulation structure effectively enhances the device stability under the ambient conditions, the additional encapsulation layers increase the overall thickness and weight of the device and compromise the flexibility. Güler et al.[36] demonstrated that the sandwich encapsulation structures increase the total device thickness from 67–235 µm to at least 316 µm. Instead, several groups directly deposited the encapsulation layer on top of devices to simplify the encapsulation structure. Weerasinghe et al.[37] encapsulated the devices with the 3M Ultra barrier solar film through lamination of the films to the front and back of the devices, and the devices kept 90% of the initial PCE after 100 h under 1-sun irradiation in an environment chamber at 60 °C and relative humidity (RH) of 50%. Previously, we utilized the flexible encapsulation films as the substrates, enabling direct deposition of the devices on the barrier films.[38] However, the hydrophobic nature of the encapsulation film impedes the deposition of the functional layers on its top, resulting in poor film quality and consequently reducing the device efficiency. Additionally, interfacial incompatibility resulted in weak interface adhesion and serious edge penetration of water and oxygen, thereby compromising the stability of devices. The previous work showed that the hydrophilic surface modifiers can significantly improve the processability of the barrier surface.[38] However, such a hydrophilic layer is detrimental to the device stability. Thus, it is crucial to develop an appropriate modification strategy to further enhance the long-term stability of FOSCs.

In this work, we presented a FOSC structure utilizing a water barrier film substrate integrated with an innovative photosensitive hydrophilic-hydrophobic conversion modification layer (NBE modification layer). This functional layer is formulated with (2-nitro-1,4-phenylene) bis (methylene) diacrylate (acrylate-NBE) as the core component, cross-linked via pentaerythritol tetra (3-mercaptopropionate) (PETMP), with Fluorolink MD700, isobornyl acrylate, with bisacylphosphine oxides phenylbis (2,4,6-trimethylbenzoyl)-phosphine oxide (BAPO) as the surfactant, reactive diluent, and photoinitiator, respectively. The introduction of the NBE modification layer significantly improved the wettability of the AgNWs inks on the hydrophobic surface and enabled the formation of uniform, large-area, flexible, transparent electrodes. After the deposition of the electrodes, the NBE layer effectively transformed from hydrophilic to hydrophobic, simultaneously strengthening the interface adhesion force. This dual functionality not only improved the air stability but also markedly enhanced the mechanical durability of the flexible OSCs. Based on this unique strategy, the FOSCs with an area of 1 cm^2 gave a champion efficiency of 16.33%. After long-term exposure of the devices to air for 600 h, the FOSCs remained ≈80% of the initial efficiency. The devices also maintained excellent stability in underwater environments. Furthermore, the device with the barrier film/NBE substrates exhibited substantial reductions in both thickness and weight compared to the conventionally stacked structure, demonstrating superior mechanical properties.

2. Results and Discussion

2.1. Comparison of Different Device Structures

Figure 1a,b illustrates the schematic diagram of the FOSCs with different encapsulation structures. The first configuration (named stack structure) employs pasting the PET/encapsulation films on the front of the device. This is the conventional method that has been widely used, involving adhering the PET/encapsulation films on the device via an extra glue, such as UV glue, with a typical thickness of tens of micrometers, and the total weight significantly increased from ≈25 to 57 mg. In contrast, the second method (named in situ structure) developed in this work involved directly fabricating the device on a barrier film substrate. This structure demonstrates the advantages of simplicity and reduced thickness, maintaining high transmittance and mechanical performance, while avoiding degradation caused by bottom adhesive encapsulation. Figure 1c exhibits the photograph of the large-scale barrier film (BF) used in this work. To determine the composition of the barrier layer, X-ray photoelectron spectroscopy (XPS) is used to analyze the elements and chemical structure. Figure S1a (Supporting Information) shows the wide scan spectra of the barrier layer, and signals corresponding to Si, N, O, C, and Na were observed. The observation of binding energy in 1071 eV from Na indicated the presence of sodium compounds on the surface of the film, which may be contaminated during operation. The core level XPS spectra of Si, N, O, and C were corrected and fitted based on the standard binding energy of the C element (284.8 eV) and shown in Figure S1b (Supporting Information). The C1s spectra mainly come from the PET substrates.[39,40] The spectra of N1s and Si2p with typical peaks at 101.19 and 398.92 eV could be attributed to the Si-N bond,[41] and the peak at 399.96 eV originated from NSi_2O.[42] Based on these results, it is determined that SiN_X and NSi_2O are the primary components of the barrier layer.

Figure 1d shows the transmittance of the barrier film and the PET film. It showed that the flexible barrier films showed similar light transmittance to the PET substrate, with a T_{550} (transmission at 550 nm wavelength) of ≈90%. The high transmission of the barrier layer would ensure a high device current of the in situ FOSCs. The stacked encapsulation structure of the PET/barrier encapsulation layer presented a lower T_{550} transmission of ≈85%. Figure 1e shows the wettability of water on the barrier film and the PET films. The water contact angle (WCA) of the barrier film surface is ≈94.7°, which is larger than the WCA of PET (64.4°). Such a high WCA of water on the top of the barrier film indicated

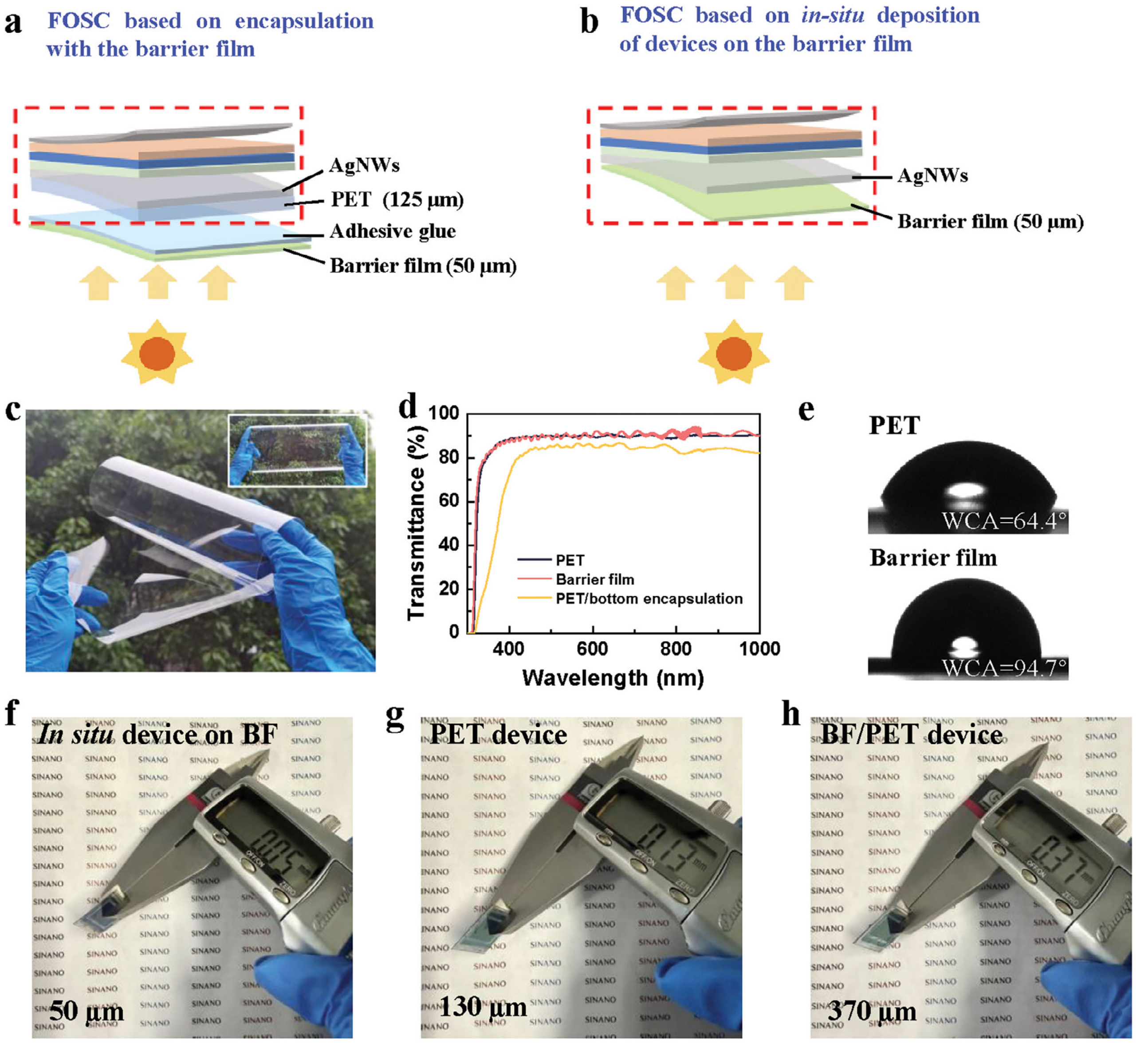

Figure 1. Characteristics of the barrier film. Schematic illustration of the in situ fabricated FOSCs device, a) using a bottom encapsulation, and b) with the barrier film substrate. c) The photograph of the barrier film. d) The transmittance spectra of PET, barrier film, and PET with bottom encapsulation. e) WCA images of PET and barrier film. f) The photograph and thickness of the FOSCs.

poor wettability of the AgNWs inks on the barrier films since the main solvent AgNWs is water. Thus, it is difficult to deposit AgNWs uniformly on the barrier film.

Moreover, we measured the thickness of devices with these different encapsulation structures and evaluated their impact on overall device thickness and weight. As shown in Figure 1f, the in situ structure exhibits an extremely low thickness of merely 50 μm. In contrast, the stack encapsulation structure, in which the barrier films are laminated onto the device surface with UV-curable adhesive, would significantly increase the device thickness. Specifically, when employing the FOSCs with a base thickness of 130 μm, the total device thickness, including the encapsulation layer, reached ≈370 μm. This result reveals that the conventional stack encapsulation architecture is inherently relatively thick, which would not only impose a significant weight increase but also compromise the device's flexibility. Conversely, the in situ structure strategy demonstrated notable advantages in weight minimization and mechanical adaptability, which overcome the critical limitations associated with traditional methodologies.

2.2. Barrier Films Modified by Hydrophilic-to-Hydrophobic Convertible NBE

As mentioned above, the barrier film exhibits high hydrophobicity; therefore, it is essential to regulate the surface energy of the barrier film to guarantee its suitability to produce transparent

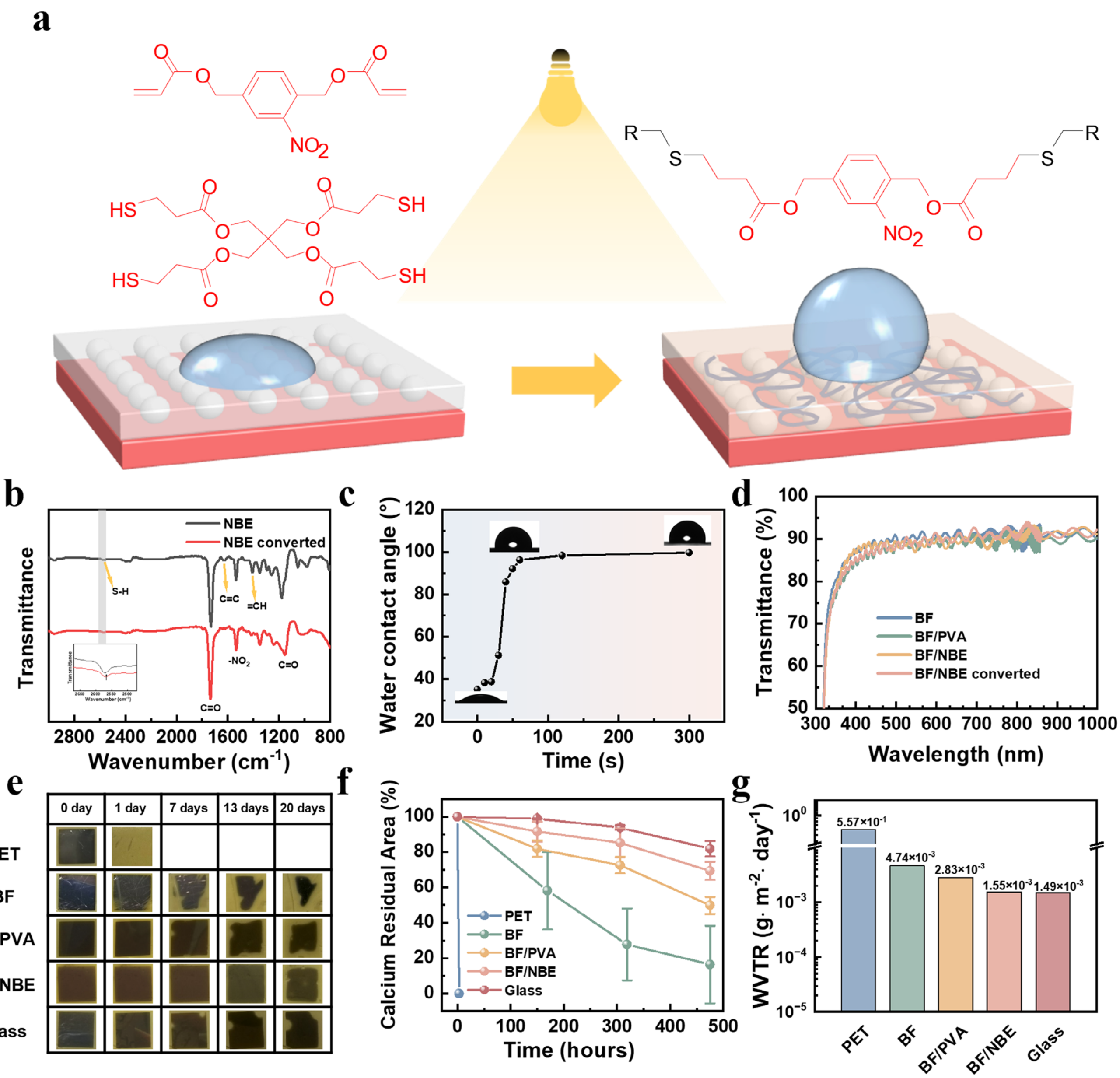

Figure 2. Structure and water vapor barrier performance of the modified layer and the unmodified film. a) Scheme diagram of NBE modified layer transforming from hydrophilic to hydrophobic. b) FT-IR spectra of the NBE modified layer before and after illumination. c) Water contact angle WCA of the NBE modified layer surface with varied LED exposure time. d) Transmittance spectra of NBE and PVA modified barrier film. e) Photographs of calcium films aged at 25 °C/100% RH. f) The residual calcium area versus aging time and g) WVTR of the different films.

electrodes and FOSCs. Interface modification using a hydrophilic material is a common method to address this issue. However, the introduction of hydrophilic material would facilitate the penetration of moisture and diminish the water barrier property of the encapsulation layer. To solve such a contradictory issue, we introduced a light conversion material, NBE, as the modifier layer. According to Rossegger et al.,[43,44] the NBE solution was prepared by mixing (2-nitro-1,4-phenylene) bis (methylene) diacrylate (acrylate-NBE), cross-linker pentaerythritol tetra (3-mercaptopropionate) (PETMP), surfactant Fluorolink MD700, reactive diluent isobornyl acrylate, with photoinitiator bisacylphosphine oxides phenylbis (2,4,6-trimethylbenzoyl)-phosphine oxide (BAPO) in chloroform solution, and the chemical structure of these compounds is shown in Figure S2 (Supporting Information). As shown in **Figure** 2a, the initial NBE-modified layer is hydrophilic. After exposure to the LED white light, the terminal carbon-carbon double bonds of acrylate-NBE and thiol groups of the functional mercaptan PETMP undergo photoinitiated addition polymerization mediated by the photoinitiator of BAPO. The reduction of numerous hydrophilic thiol groups during this reaction induces a gradual transition of the film from hydrophilic to hydrophobic. Similar results have been reported in previous works.[43–45] Actually, the hydrophilic-to-hydrophobic surface conversion can also be achieved under the illumination of UV light (Figure S3, Supporting Information). Because the white LED lamp is relatively common and easily accessible, we used the white LED lamp as the illumination source.

Hydrophilic modification of the barrier layer is beneficial in improving the uniform distribution of the AgNWs, while the hydrophobic property will help to block the penetration of water vapor. To determine the polymerization reaction process during the hydrophobic transformation, Fourier Transform infrared spectroscopy (FT-IR) of the films was measured before and after light exposure. As shown in Figure 2b, the absorption bands at 1630–1660 and 1400–1420 $\mathrm{cm^{-1}}$ became much weaker after light conversion, indicating the decline of the C = C and = CH. Also, a decrease of the thiol peak at 2670 $\mathrm{cm^{-1}}$, ascribing to the breakage of S-H bonds, is observed, which points to the polymerization reaction of mercaptan and acrylate-NBE. The FT-IR results proved the occurrence of mercaptan polymerization. The time-dependent FT-IR spectra of the films during 3 min of light illumination are shown in Figure S4 (Supporting Information). As illustrated in Figure S4a (Supporting Information), the absorption peaks intensity corresponds to C = C and = CH stretching at 1630–1660 $\mathrm{cm^{-1}}$ and 1400–1420 $\mathrm{cm^{-1}}$ gradually decrease as the irradiation time increases. Similarly, Figure S4b (Supporting Information) shows a continuous decrease of the -SH peak as the illumination time increases. These results confirm that the additional reactions between thiol groups and carbon-carbon double bonds occur progressively under light exposure, leading to the hydrophilic-to-hydrophobic transformation. The converting efficiency could be estimated according to the FT-IR spectra, and the result showed an increase in converting efficiency from 37% to ≈50% with illumination time increased from 20 to 80 s, and kept ≈50%–56% with illumination time increased further (the detailed value listed in Table S1, Supporting Information). Since the converting efficiency is not very high, it is reasonable to speculate that the hydrophilic-to-hydrophobic converting mainly occurred at the surface of the films, and the inner films will not totally convert.

The change of surface energy during the hydrophilic-to-hydrophobic conversion process was studied through water contact angle (WCA). Figure 2c depicts the evolution of WCA of the NBE-modified layer during light exposure. It showed that the WCA increases rapidly from 30° to 100°° with the increase of exposure time within 90 s, and remains nearly ≈100° in the following 5 min. This observation agrees with the FI-IR results, indicating that the conversion efficiency will not largely change after 90 s. Meanwhile, the relationship between the thicknesses of NBE and surface free energy (Figure S5, Supporting Information) reveals that a thicker NBE film would enable a higher surface energy of the pristine films, but a lower surface energy of the converted films. To ensure suitable modification films with proper surface energy for AgNWs deposition and keep long-term stability, a film around an appropriate thickness of 60 nm was used as an optimized modification layer. Figure 2d shows the transmittance spectra of the modification layer before and after conversion. The T_{550} of the NBE-modified barrier film is 87.3%, which is slightly lower than the unmodified barrier film (90.1%), while it increased to 89.2% after hydrophilic-to-hydrophobic conversion of NBE. These results showed that the difference of T_{550} between the unconverted NBE-modified layer and the hydrophilic-to-hydrophobic converted film is ≈1.7%. In addition, the UV–vis absorption spectra of the films showed no change after hydrophilic-to-hydrophobic conversion (Figure S6, Supporting Information); therefore, this might suggest that the conversion process itself has minimal impact on the optical transmittance of the films. Here, the slight change of T_{550} might be due to the deviations of interference since the obvious interference fingers have been observed. Thus, the hydrophobic NBE layer is suitable for substrate modification with negligible transmission loss (Figure S6, Supporting Information). Since PVA is a commonly used modification layer, the PVA modification is also fabricated as a comparison in this work. It demonstrated that the PVA-modified barrier film showed a similar T_{550} of 88.2% compared to the original film.

To determine the impact of interfacial modification on the barrier performance, an optical calcium film measurement was carried out to determine the water vapor transmission rate (WVTR), which relies on the fact that the opaque calcium film becomes transparent upon reacting with water or oxygen molecules to form $\mathrm{Ca(OH)_2}$ and/or CaO.[46] The schematic illustration of the fabrication process for observable calcium film samples is shown in Figure S7 (Supporting Information). In this work, three individual samples were prepared for this measurement. Figure 2e shows the typical photographs of calcium films on different substrates during aging at 25 °C/100% relative humidity (RH) within 20 days. To calculate the calcium film area accurately, we first measured the discernible calcium area via optical images. The temporal evolution of the residual calcium film area with the corrosion rate derived from linear fitting of the residual area versus time curve is plotted in Figure 2f. It shows that the corrosion rate of the PET sample is significantly quicker, while that of the BF/PVA and BF/NBE samples is much slower. In detail, the calcium film was completely corroded within 3 h for the pristine PET film, the pristine BF, BF/PVA, and BF/NBE film showed 16.3% ± 21.2%, 49.8% ± 4.9%, and 69.4% ± 5.1% remaining area after 20 days of corrosion. It should be noted that for the bare BF substrate, two samples were nearly corroded in the end, thereby the error bar is much larger than other films. To quantitatively compare the difference between NBE and PVA modification, the WVTR of different substrates was calculated via the calcium corrosion method. In this method, WVTR is defined as the corrosion rate of the calcium film under controlled humidity conditions, calculated using the following equation:[47]

$$WVTR\ \left(g \cdot m^{-2} \cdot day^{-1}\right) = n \times \delta_{Ca} \times \frac{M\left(H_2O\right)}{M\left(Ca\right)} \times h \times \frac{dA}{dt} \times \frac{1}{A} \qquad (1)$$

Here $n = 2$, which is the molar ratio of water to calcium in the calcium oxidation reaction, δ_{Ca} is the calcium density (1.55 $\mathrm{g\ cm^{-3}}$), $\mathrm{M(H_2O)}$ and M(Ca) are the molar masses of water and calcium. Meanwhile, h, dA/dt, and A represent calcium thickness, the area reduction rate of calcium film, and the area of evaporated calcium, respectively. According to Equation 1, the average WVTR of the different substrates based on three individual samples (Figure 2g) was calculated. As shown in the figure, the PET substrate showed a relatively high WVTR of 5.6 × 10^{-1} $\mathrm{g\ m^{-2}\ day^{-1}}$. In contrast, the barrier film exhibited a low

WVTR of 4.7×10^{-3} g m^{-2} day^{-1}. After PVA modification, the WVTR of the barrier film was reduced to 2.8×10^{-3} g m^{-2} day^{-1}. The NBE modification further reduced the WVTR of the barrier film to 1.5×10^{-3} g m^{-2} day^{-1}, indicating that the hydrophilic-to-hydrophobic modification strategy is an effective method to promote the water and oxygen barrier ability of the barrier film.

Furthermore, the photographs of the calcium films clearly showed that corrosion initially started at the edges, with subsequent corrosion occurring in a gradual, inward direction, indicating that moisture ingress is primarily an edge-driven corrosion process. Notably, the pristine barrier film showed significant corrosion after 20 days immersion test. Quantitative analysis revealed that ≈2/3 of the films were corroded. However, the central region nearly maintained its original morphology without visible corrosion, suggesting edge-induced corrosion. In contrast, the NBE-modified film exhibited less corrosion and nearly no moisture entering from the edges. These results could be ascribed to the enhancement of adhesive force between the NBE-modified barrier film and substrates. The surface adhesion of the modified layer on the barrier film was measured by peeling adhesive tape, and the results are presented in Figure S8 (Supporting Information). It was found that the surface adhesion of the NBE-modified barrier film is significantly enhanced compared to the unmodified barrier film, with the maximum peeling load increasing from 0.54 to 0.72 N. Such an increased surface adhesion would contribute to strengthening of bond force between the barrier layer and the AgNWs electrode. In contrast, the BF/PVA film exhibits moderate enhancement in surface adhesion, with a maximum peeling load of 0.66 N. However, as the displacement increases, the load decreases to 0.43 N and then rises again to 0.64 N, indicating non-uniform adhesion.

2.3. AgNWs Flexible Transparent Electrode on the NBE-modified Barrier Films

With the NBE-modified barrier layer as the substrate, the flexible transparent AgNWs electrodes were fabricated, and the SEM images are shown in **Figure** 3a–i. As a comparison, the PVA modifier was also studied. The morphology of the AgNWs electrodes on the pristine barrier films (named BF/AgNWs) exhibited extreme inhomogeneity (Figure 3a–c), which is consistent with the non-wetting nature of AgNWs inks on the barrier films. The films of AgNWs on the PVA, named BF/ PVA/ AgNWs (Figure 3d–f), showed localized, non-uniform morphology, and Figure 3g–i showed that the films of AgNWs on the NBE (BF/NBE/AgNWs) had homogeneous morphology without obvious aggregation. These SEM results demonstrated that PVA and NBE modification enhanced the quality of AgNWs electrode fabricated on top of barrier films. Specifically, NBE significantly improved the processability, yielding BF/NBE/ AgNWs electrodes with superior morphological uniformity compared to the PVA modified substrate. Figure 3j–l illustrates schematic diagrams of the three electrodes. Generally, the AgNWs electrode was comprised of three typical regions: large, uncovered regions, partially uncovered small regions, and uniformly covered regions. The coverage of the AgNWs on different substrates was estimated to be ≈51.2%, 70.5%, and 75.8% based on the SEM images (Figure S9, Supporting Information). The SEM images of the BF/NBE/AgNWs films before and after light exposure were measured to evaluate the influence of hydrophilic-to-hydrophobic conversion. The result confirmed that there were no significant changes in the AgNWs morphology after hydrophilic-to-hydrophobic conversion (Figure S10, Supporting Information). The AFM images of flexible electrodes are shown in Figure S11 (Supporting Information). The AgNWs covered region exhibited RMS ≈14.6, 12.7, and 12.0 nm for the BF/AgNWs, BF/PVA/AgNWs, and BF/NBE/AgNWs electrodes, respectively.

As shown in Figure S12 (Supporting Information), both the sheet resistance and transmittance of the AgNWs electrodes are dependent on the thickness of the AgNWs. To achieve an electrode with low sheet resistance and high transmission, we selected a thickness of ≈50 nm as the optimal value. Figure 3m shows the transmittance spectra of these AgNWs electrodes. The T_{550} of the barrier film electrode without modification is ≈82.0%. BF/PVA/AgNWs and BF/NBE/AgNWs electrodes revealed T_{550} of ≈80.7% and 79.4% respectively. These AgNWs on the BF showed an average T_{550} of 80.7%, like the T_{550} of PET/AgNWs (80.9%) (Figure S13, Supporting Information). For these electrodes, the average sheet resistance is 13.0, 14.0, and 13.9 Ω sq^{-1} for the BF/AgNWs, BF/PVA/AgNWs, and BF/NBE/AgNWs electrodes, respectively (Figure S14, Supporting Information).

The flexibility and adhesion of the flexible transparent electrodes are critical to the application of the flexible electrodes for FOSCs. Figure 3n shows the adhesive force of NBE, PVA-modified electrodes, and the pristine electrode. After 300 times cyclic stick-peel with 3 M tape, the sheet resistance of the BF/AgNWs electrode increases by 1.1 times higher than the initial. While the sheet resistance of BF/PVA/AgNWs electrodes has little change, the BF/NBE/AgNWs electrode even showed 10% reduction of sheet resistance after stick-peel cycles. It is speculated that the surface of AgNWs electrodes has good adhesion to the modified layer, which proves to peel off the impurities from the barrier film. Figure 3o and Figure S15 (Supporting Information) show the evolution of sheet resistance and transmittance at 550 nm of the flexible electrodes during bending. After 10000 times bending cycles, the sheet resistance of BF/NBE/AgNWs electrode only increased to 1.07 times the initial value, while the sheet resistance of BF/AgNWs and BF/PVA/AgNWs increased to 1.15 and 1.31 times of the initial value. This result demonstrates improved bending resistance of the electrode on the NBE-modified layer. The mechanical properties of flexible electrodes are primarily determined by three factors: the substrate, the thin film, and the adhesion strength between the substrate and the film. In this work, the use of NBE significantly enhances interfacial adhesion between the AgNWs and the BF substrates (Figure 3i), which would be the main reason for improved mechanical performance of the NBE-based electrode. The T_{550} of BF/AgNWs decreased from 81% to 78%, that of the BF/PVA/AgNWs electrode decreased from 80% to 77%, and the BF/NBE/AgNWs decreased from 79% to 77%. The reduction of T_{550} during bending might be due to an increase in scattering since continuous bending would cause slight cracks in the substrates and the barrier layer, like the reported result.[48] Therefore, all the electrodes exhibited nearly comparable decline in transmittance.

In addition, we investigated the ambient stability of electrodes. The electrodes were stored in an ambient with a

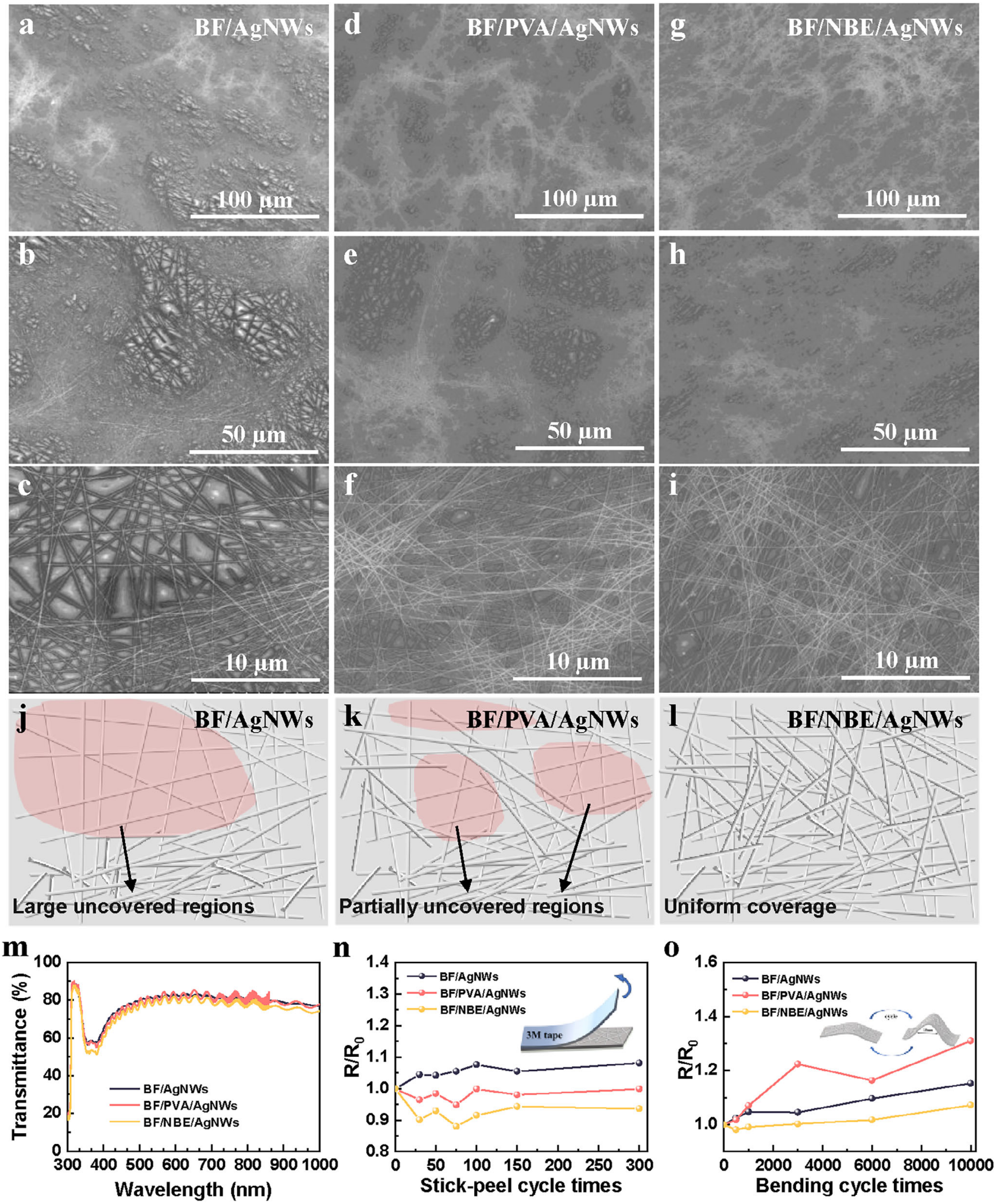

Figure 3. The SEM images of a–c) the BF/AgNWs, d–f) BF/PVA/AgNWs, g–i) BF/NBE/AgNWs. Schematic illustration of j) BF/AgNWs, k) BF/PVA/AgNWs, l) BF/NBE/AgNWs with different coverage of AgNWs. m) The transmittance spectra of the BF/modified layer/AgNWs electrodes. Variation in sheet resistance during n) 300 stick-peel cycles with 3 M tape, and o) 10000 continuous bending cycles of the three varieties of barrier film electrodes.

Table 1. Photovoltaic parameters of 1 cm^2 FOSCs based on different electrodes under the illumination of 100 mW cm^{-2}.

Active layer	Electrode	V_{OC} [V]	J_{SC} [mA/cm^2]	FF [%]	PCE [%]
PM6:L8-BO	PET/AgNWs	0.890	24.22	74.72	16.11
		0.886 ± 0.003	23.97 ± 0.40	74.23 ± 0.56	15.77 ± 0.26
	BF/PET/AgNWs	0.899	21.83	72.14	14.16
		0.871 ± 0.037	22.05 ± 0.73	72.59 ± 0.85	13.92 ± 0.22
	BF/AgNWs	0.810	22.30	50.03	9.03
		0.427 ± 0.229	21.97 ± 0.32	34.21 ± 11.02	3.60 ± 3.18
	BF/PVA/AgNWs	0.890	23.10	74.17	15.25
		0.889 ± 0.002	22.86 ± 0.46	72.98 ± 1.77	14.83 ± 0.50
	BF/NBE/AgNWs	0.890	23.11	74.26	15.28
		0.889 ± 0.002	22.73 ± 0.43	73.88 ± 0.94	14.92 ± 0.29
	Glass/ITO	0.872	26.15	70.96	16.18
		0.872 ± 0.003	25.08 ± 0.67	71.05 ± 0.78	15.54 ± 0.40
PM6:BTP-BO-4Cl:C-$PC_{61}BM$	PET/AgNWs	0.824	27.28	72.92	16.39
		0.826 ± 0.002	27.02 ± 0.23	71.62 ± 0.84	15.99 ± 0.26
	BF/PVA/AgNWs	0.814	27.41	73.71	16.45
		0.813 ± 0.002	26.05 ± 0.92	73.55 ± 0.61	15.58 ± 0.62
	BF/NBE/AgNWs	0.813	26.75	75.08	16.33
		0.818 ± 0.005	26.41 ± 0.57	73.69 ± 1.2	15.91 ± 0.38

humidity ≈50%, and sheet resistance and transmittance were measured periodically over 20 days (Figures S16 and S17, Supporting Information). As a result, the sheet resistance of the BF/AgNWs, BF/PVA/AgNWs, and BF/NBE/AgNWs electrode increased to 1.22, 1.15, and 1.09 times of the initial value, respectively. These results demonstrated that surface-modified samples show a smaller variation of sheet resistance than the control film, indicating minimal degradation of the electrodes. For the light transmission, all the samples showed ≈1% decrease in T_{550}. XPS results of Ag 3d (Figure S18, Supporting Information) showed a shift of bending energy from 367.85 eV to 368.45, 367.95, and 368.00 eV for the aged BF/AgNWs, BF/PVA/AgNWs, and BF/NBE/AgNWs electrodes, which could be ascribed to the surface oxidation of AgNWs.[49] However, a smaller shift of binding energy of BF/NBE/AgNWs and BF/PVA/AgNWs than the BF/AgNWs electrodes was observed, demonstrating that the surface-modified substrates enabled higher ambient stability. Although AgNWs electrode showed a slight increase in sheet resistance, the fluctuation of the conduction within an acceptance range has minimal impact on the device performance. Furthermore, the metal oxide interface and active layer deposited on top of the electrodes in the FOSCs device would protect the AgNWs electrode.

In addition, the UV stability of the electrodes was investigated, and the electrodes were exposed to UV irradiation (using 365 nm as the light source, with intensity of 680 mW cm^{-2}) under the condition of 25 °C and 50% HR from front (irradiated from the substrate side) and back irradiation (irradiated from the AgNWs side) (Figures S19 and S20, Supporting Information). We found the electrodes showed a smaller change of sheet resistance from top irradiation than from back irradiation, indicating, the oxidation of Ag is a main reason for the UV degradation rather than the substrate. For the front irradiation, a negligible change in sheet resistance was observed. The transmittance spectra of the electrodes and substrates proved this speculation (Figure S21, Supporting Information). For applications of FOSCs, irradiation typically occurs from the front side, while the back side is encapsulated. Therefore, under real operational conditions, the performance degradation under UV irradiation caused by the flexible substrate and electrode is not a big problem in the short term. Whatever, for long-term UV stability, the degradation problem of the PET substrate is still a big issue that needs to be solved.[50,51] In addition, several works have demonstrated that the most critical issue to be addressed for the UV stability of FOSCs is the interfacial layer.[52,53]

2.4. Devices: Performance of In Situ Fabrication on the Barrier Film

To evaluate the performance of FOSCs based on barrier film substrates, 1 cm^2 FOSCs were fabricated on the different substrates, with PM6, L8-BO, and BTP-BO-4Cl: cross-linkable-$PC_{61}BM$ (C-$PC_{61}BM$) as donor and acceptor. **Figure** 4a shows the device structure and chemical structures of the organic donor and acceptor. The *J–V* characteristics of PM6:L8-BO FOSCs on the different electrodes are shown in Figure 4b, and detailed photovoltaic parameters are listed in **Table** 1. The reference devices with PET/AgNWs electrodes exhibited an optimal open circuit voltage (V_{OC}) of 0.890 V, a short circuit current density (J_{SC}) of 24.22 mA cm^{-2}, and a fill factor (FF) of 74.72%, resulting in a power conversion efficiency (PCE) of 16.11%. For the conventional encapsulation method, the barrier layer is laminated on the front of the devices. After encapsulation, both the J_{SC} and FF are significantly reduced, and finally, the device's PCE is reduced to 14.16%. This result indicated the necessity of in situ fabricating the device on top of the barrier film substrate.

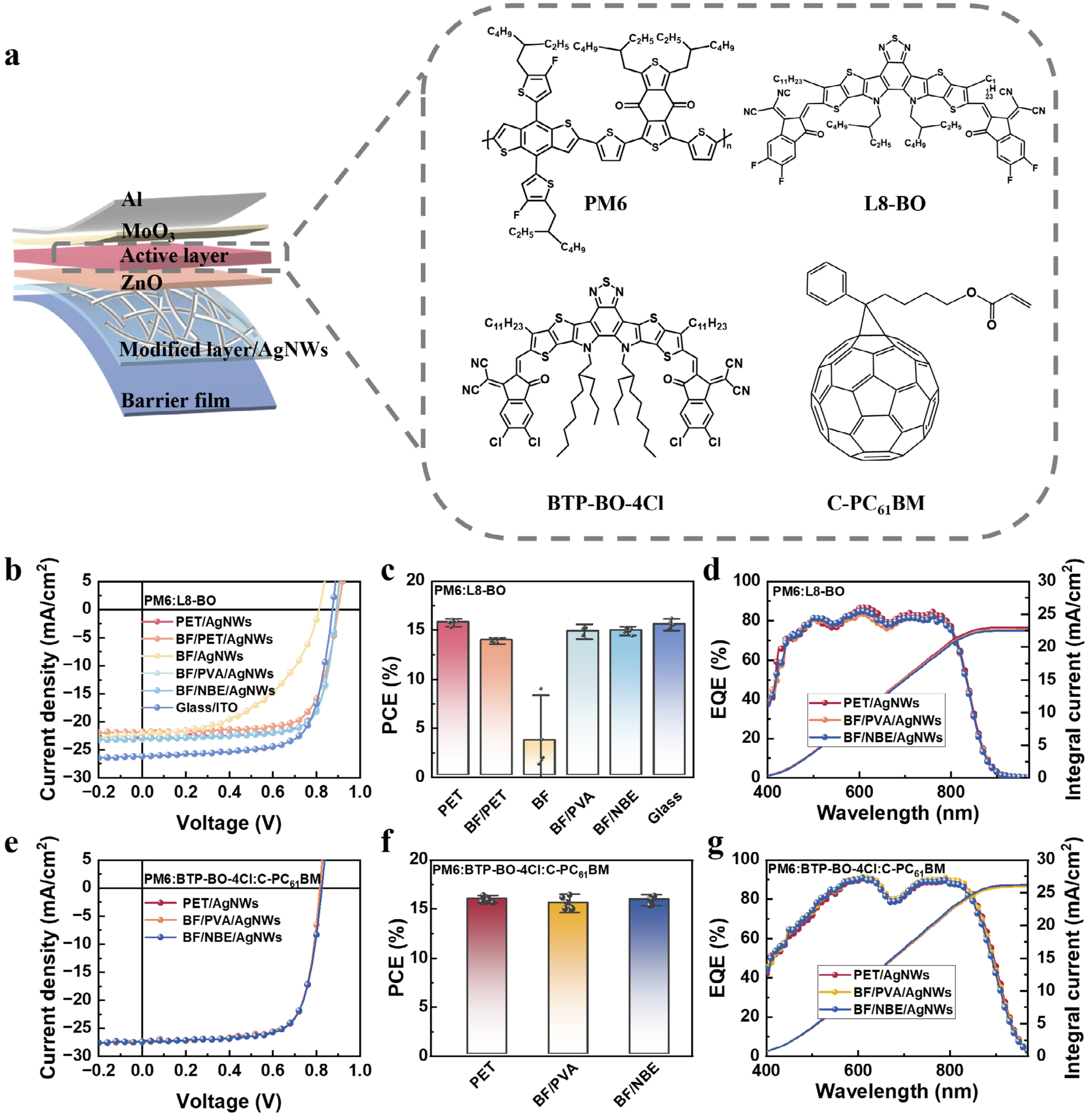

Figure 4. The structure and performance of the 1 cm^2 FOSCs. a) Schematic structure of the FOSCs with a barrier film, the chemical structures of PM6, L8-BO, BTP-BO-4Cl, and C-PC$_{61}$BM. b) *J–V* characteristics, c) statistical chart of PCE, and d) EQE of the PM6: L8-BO FOSCs on different substrates. e) *J–V* characteristics, f) statistical chart of PCE, and g) EQE spectra of the PM6: BTP-BO-4Cl:C-PC$_{61}$BM FOSCs on different substrates.

For the device in situ fabricated on the barrier layer, the poor wettability of the barrier layer film hindered the successful preparation of the AgNWs electrode. After plasma treatment, the surface energy of the barrier film allows for the deposition of AgNWs. However, the devices based on the BF/AgNWs electrodes are still low, showing the best PCE of 9.03% with a V_{OC} of 0.810 V, a J_{SC} of 22.30 mA cm^{-2}, and an FF of 50.03%, and only gave an average PCE of 3.6 ± 3.18%. Such a low performance, particularly the reduced V_{OC} and FF could be attributed to severe current leakage or even device short circuit, resulting from electrode unevenness. With the PVA and NBE modified barrier layer substrates, the device performance was greatly improved to ≈15%. In detail, the PVA-modified devices gave the best PCE of 15.25%, with V_{OC} of 0.890 V, J_{SC} of 23.10 mA cm^{-2}, and FF of 74.17%. NBE-modified devices showed a best PCE of 15.28%, with a V_{OC} of 0.890 V, a J_{SC} of 23.11 mA cm^{-2}, and an FF of

74.26%. The rigid device based on the glass/ITO electrode exhibited a V_{OC} of 0.872 V, a J_{SC} of 26.15 mA cm^{-2}, and an FF of 70.96%, resulting in a PCE of 16.18%. The histogram of device PCE on different substrates is shown in Figure 4c. The unmodified barrier film-based devices exhibited relatively poor performance and wide PCE distribution. In contrast, the performance of the barrier film devices was substantially improved after surface modification, as evidenced by enhanced PCE and a more stabilized distribution. In addition, the EQE of FOSCs is consistent with the J_{SC} values of the J–V tests (Figure 4d). These results exhibited that the devices fabricated using PVA and NBE modification have comparable performance to those based on the conventional PET-based device. This indicates the hydrophilic surface treatment of the hydrophobic barrier layer is effective to enhance the processability.

Besides the PM6:L8-BO FOSCs, PM6:BTP-BO-4Cl:C-PC$_{61}$BM ternary devices were also fabricated. The J–V characteristics of the PM6:BTP-BO-4Cl:C-PC$_{61}$BM devices are shown in Figure 4e, and detailed photovoltaic parameters are listed in Table 1. The flexible device with PET/AgNWs electrode exhibited a best PCE of 16.38%, with a V_{OC} of 0.824 V, a J_{SC} of 27.28 mA cm^{-2}, and a FF of 72.92%. The BF/PVA/AgNWs and BF/NBE/AgNWs-based devices exhibited an optimal PCE of 16.45% and 16.33%, respectively. In detail, the PVA-modified devices gave the best V_{OC} of 0.814 V, J_{SC} of 27.41 mA cm^{-2}, and FF of 73.71%, and the NBE-modified devices gave a similar best V_{OC} of 0.813 V, J_{SC} of 26.75 mA cm^{-2}, and FF of 75.08%. In this photoactive system, we also observed that the devices on the barrier films exhibited slightly lower V_{OC} compared to those on bare PET substrates. This might be primarily from the rougher AgNWs on the barrier films, which leads to slightly higher interface recombination. In addition, for the BF/PVA/AgNWs and BF/NBE/AgNWs device, slightly larger V_{OC} variation and error bar were observed in this ternary system than in the PM6:L8-BO binary photoactive system. In this work, the PM6:BTP-BO-4Cl:C-PC$_{61}$BM ternary active layers were annealed at 150 °C for 30 min to form a crosslinked active layer, as reported in our previous work.[54] During such a long time of high-temperature annealing, the morphology of the active layer and the interfaces between the active layer and the interface layer may show variation. This might be the main reason for the relatively large error bar of $V_{OC.}$ The histogram of PCE in Figure 4f reveals a more concentrated distribution for PET and BF/NBE-based devices, whereas BF/PVA devices display significantly broader dispersion. As shown in Figure 4g, the EQE of the FOSCs is consistent with the J_{SC} values of the J–V results.

2.5. Stability of the FOSCs Based on In Situ Fabrication on the NBE-Modified Barrier Film

With these flexible and rigid devices, the long-term stability was systematically studied. Both the rigid and flexible devices on the PET and barrier film substrates are stored in the air without encapsulation. J-V curves were periodically measured during 400 h of aging, and the evolution of PCE is shown in **Figure 5**a. It can be observed that the rigid devices retained 54% of the initial PCE after 383 h, while the PET devices exhibited poorer stability, retaining only 31% of their initial efficiency. The BF/NBE devices kept 57% of the initial PCE even without any encapsulation, which is higher than rigid devices. BF/PVA devices maintained 48% of the initial PCE and were nearly comparable to the rigid glass. In detail, the evolution of V_{OC}, J_{SC}, FF, and PCE of different FOSCs during 400 h storage in the air is shown in Figure S22 (Supporting Information). The results illustrated that the V_{OC} values of these four types of devices followed a similar change trend over the 383 h storage duration, and remained 90% of the initial V_{OC} after 383 h. The NBE-modified barrier film devices exhibited a slower decline in J_{SC}, with 92% remaining initial J_{SC}, similar to that of the rigid one. And BF/NBE devices also demonstrated improved stability in FF, keeping 65% of the initial value. These results indicated that the BF/NBE substrates worked well like the rigid device. Based on these results, we can foresee that if we can effectively encapsulate the top side, it is possible to obtain highly stable FOSCs that work in the air.

Meanwhile, the long-term stability of the top encapsulated devices was also measured, and the results are shown in Figure 5b. We can observe the PET devices degrade to 30% of the initial PCE after 334 h of aging. The PVA-modified devices degraded to 62% of the initial PCE. The rigid devices and the BF/NBE devices retained 86% and 77% of the initial PCE after 600 h of aging. This result demonstrated that the BF/NBE devices have higher air storage stability than the PVA-modified device. In addition, the comparable shelf stability of the FOSCs to the rigid device suggested that the degradation of FOSCs caused by the plastic substrates could be addressed by using the NBE-modified barrier substrates. According to the results of Figure S23 (Supporting Information), the V_{OC} values of these devices showed minimal variation; the variation of J_{SC} of BF/NBE devices was nearly unchanged, close to the glass devices, and J_{SC} of PET-based devices only kept 64% after storage for 334 h. This observation demonstrated that the use of BF/NBE is a highly effective approach for preserving J_{SC} stability.

In addition, we also tested the stability of flexible devices in water. As shown in Figure 5c, the devices based on BF/PVA maintained 67% (average value of (65 ± 3)%) of the initial PCE, and BF/NBE devices maintained 98% (average value of (94 ± 5)%) of their initial efficiency after soaking in water for 4 h, while the PET device degraded to 26% (average value of (11 ± 13)%) of the initial performance after the same condition. Here, we found a slight increase in PCE for the BF/NBE/AgNWs devices ≈2–3 h. Among the performance parameters, both J_{SC} and FF showed a slight increase. Thus, it might be ascribed to low temperature and better light transmission in the presence of water. Such interesting results have been reported by Someya et. al.[26] and Hou et. al.[55] However, because the devices degraded quickly of BF/AgNWs devices, the positive contributions of the above effects do not manifest. These results demonstrate that the hydrophilic-to-hydrophobic modification strategy is feasible to improve processability and device efficiency, and meanwhile significantly enhances the device stability, representing a dual-functional effect.

Furthermore, we investigated the mechanical durability of the flexible devices during continuous bending with a radius of 5 mm, and the results are shown in Figure 5d. The devices with PET substrate exhibited 90.0% remaining PCE after 1 0000 times bending cycles. The BF/PVA/AgNWs and BF/NBE/AgNWs devices kept 96% and 95% of the initial PCE. As previously mentioned, the sandwich encapsulation structure is currently widely used for device encapsulation. However, the additional barrier

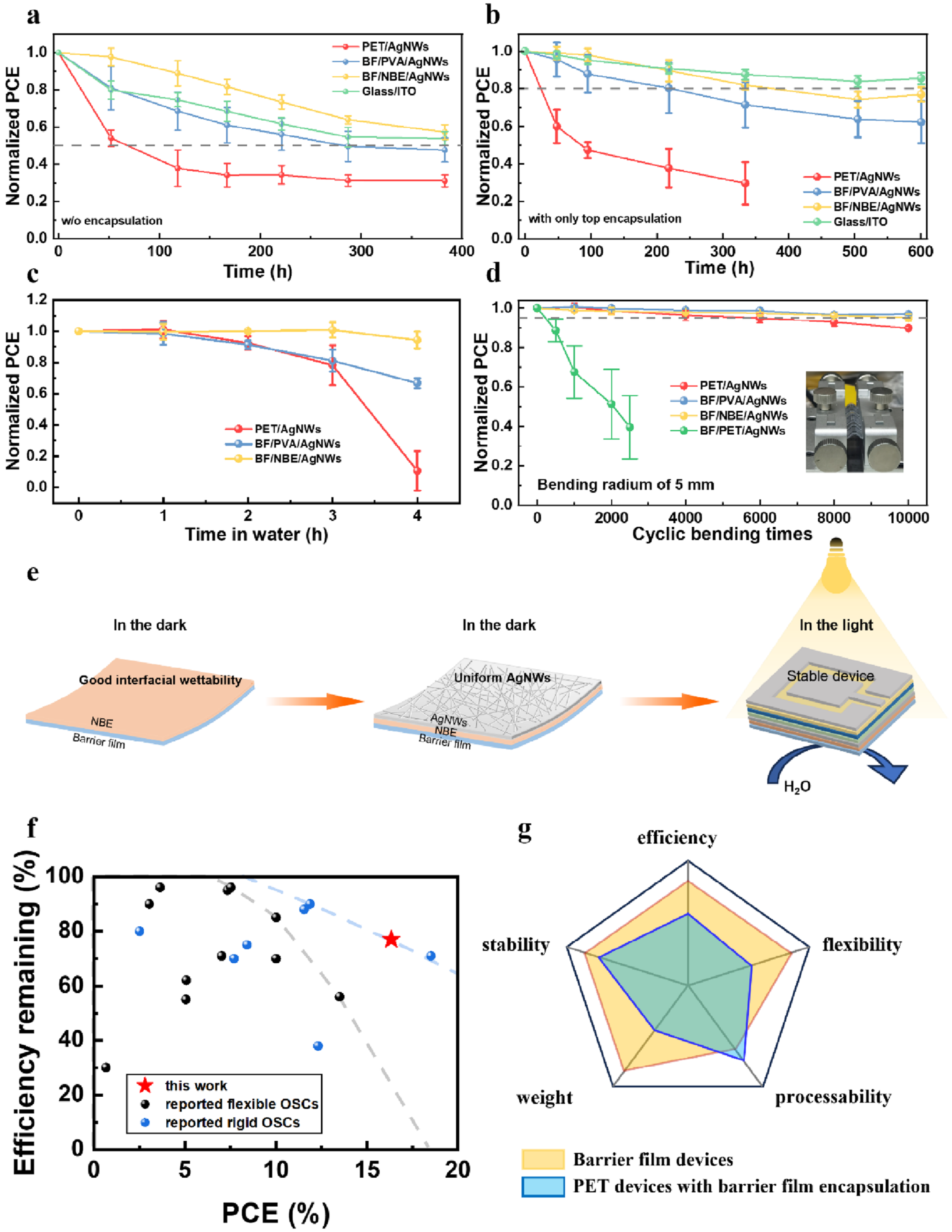

Figure 5. The air stability of the FOSCs. a) w/o encapsulation and b) with only top encapsulation. c) Stability of the FOSCs in water. d) The evolution of PCE during the continuous 10000 times bending with a bending radius of 5 mm. e) Schematic illustration of stable device fabrication and working principle of the hydrophilic to hydrophobic conversion. f) Summary of air storage stability of the OSCs.[29,37,38,56–66] g) The parameters comparison for barrier film devices (yellow area) and PET devices with barrier film encapsulation.

layers and adhesive layers, i.e., UV glue in this structure, adversely affect both device thickness and mechanical properties. As illustrated in Figure 5d, device performance employing sandwich encapsulation sharply decreased after 2500 bending cycles, demonstrating its incompatibility with flexible electronics. The evolution of other parameters is shown in Figure S24 (Supporting Information). The V_{OC} and J_{SC} values of these types of FOSCs devices showed nearly consistent. The FF of PET reference devices exhibited relatively quicker reductions with keeping 94% initial value, while BF/PVA and BF/NBE devices remained over 97% and showed higher stability during the continuous 10000 times bending. This result means the interface damage during bending was successfully suppressed. The PET devices with top encapsulation exhibited noticeable degradation in V_{OC}, J_{SC}, and FF. Among these parameters, FF showed the most pronounced decline, leading to a substantial reduction in PCE. The schematic illustration of the fabrication and working principle of a stable barrier film device is shown in Figure 5e. The pristine NBE-modified layer helped to enhance wettability between the AgNWs inks and the barrier film, and the hydrophobic surface of the NBE layer after light exposure is beneficial for preventing moisture permeation and improving the device stability.

Figure 5f summarizes the long-term shelf stability of OSCs stored in air reported in the literature, and the detailed data are provided in Table S2 (Supporting Information). We can see for the organic system, most of the FOSCs remained ≈60% of the initial efficiency after 20 days of storage in air. Limited works have reported long-term stability in the low-performance organic systems, such as PTB7:$PC_{70}BM$.[56] In contrast, the device with efficiency higher than 15% always gave unsatisfactory long-term stability. In this work, the FOSCs based on BF/NBE achieved a high PCE of 16.33% for the 1 cm^2 device, along with an excellent stability comparable to that of the rigid OSCs. These results strongly demonstrate the significant role of the NBE-modified barrier film in enhancing the stability of FOSCs.

Figure 5g exhibits a comparative analysis of the key parameter attributes between the barrier film devices (yellow area) and the PET devices encapsulated with barrier film (blue area). For the FOSCs, efficiency, mechanical flexibility, processability, weight, and operational stability are the five critical metrics. Based on our results, we see that the PET-encapsulated devices demonstrated comparable processability and stability to the in situ barrier devices. While the in-situ barrier devices achieved remarkable comprehensive performance relative to the conventional encapsulated devices: reducing weight by 50%, enhancing efficiency by at least 10%, maintaining stability under air conditions, and preserving excellent flexibility with a bending radius of 5 mm. This holistic performance suggests in situ barrier technology as a superior solution for lightweight, high-efficiency, and durable FOSCs.

3. Conclusion

In this work, highperformance and long-term stable FOSCs were developed with barrier film as substrates and an innovatively utilized a light-sensitive material, NBE, as the interface modification layer. In this structure, the NBE material plays two critical roles. First, with the hydrophilic NBE as the modifier of the barrier film, the nonwetting issue of the AgNWs inks was solved, which enabled the fabrication of uniform AgNWs electrodes on the barrier film. Second, after converting from hydrophilic to hydrophobic NBE, the NBE modification layer further decreased the WVTR of the barrier film. The FOSCs with barrier film/NBE substrates achieved an optimized PCE of 16.33% and retained ≈80% of their initial value after being stored in the air for 600 h, which is close to the 86% retention observed in the rigid devices. Moreover, the FOSCs maintained long-term stability underwater. Furthermore, due to the simple and thin structure, the FOSCs with barrier film/NBE substrates exhibited excellent mechanical properties.

4. Experimental Section

Materials: AgNWs inks (3.2 mg mL^{-1} in H_2O and IPA with an average diameter of 25 nm and a length of 25 µm) were purchased from Tianjin Naibo New Material Technology Co., Ltd. PM6 was purchased from Hyper Inc. L8-BO was purchased from Hyper Inc. 1,4-Dichlorobenzene (DIB) was purchased from TCI Co. BTP-BO-4Cl was purchased from Hyper Inc. C-$PC_{61}BM$ was synthesized by Shanghai Institute of Organic Chemistry (SIOC).[67] 1-Bromo-3,5-dichlorobenzene (DCBB) was purchased from Shanghai Titan Scientific Co., Ltd. C_{60} SAM (4-(1′,5′-Dihydro-1′-methyl-2′H-[5,6] fullereno-C_{60}-IH-[1,9-c] pyrrol-2′-yl) benzoic acid) was purchased from J&K Scientific. PVA was purchased from Anhui Wanwei Group Co. The photoinitiator phenyl bis(2,4,6-trimethylbenzoyl)-phosphine oxide (BAPO), Pentaerythritol tetra(3-mercaptopropionate) (PETMP) was purchased from TCI Co. Fluorolink MD700 was supplied by Foshan Zhaojing Environmental Protection Technology Co., Ltd. Isobornyl acrylate was purchased from Shanghai Titan Scientific Co., Ltd. (2-nitro-1,4-phenylene) bis (methylene) diacrylate(acrylate-NBE)was synthesized by our group. Chloroform (CF) was purchased from Yonghua Chemical Co. Ltd.

Fabrication of Flexible Transparent Electrodes: The NBE solution was prepared by dissolving the acrylate-NBE (10.00 mg, 0.034 mmol, 37.5 mol%), isobornyl acrylate (7.15 mg, 0.034 mmol, 37.5 mol%), PETMP (11.18 mg, 0.023 mmol, 25.0 mol%), Fluorolink MD700 (0.29 mg, 1.0 wt.%), and BAPO (0.73 mg, 2.5 wt.%) in 1 mL chloroform and ultrasonic vibrated for 3 min as described in our previous work.[45] The PVA solution with concentration of 0.5 mg mL^{-1} was prepared by dissolving the PVA in deionized water and was stirred at temperature of 90 °C for at least 12 h. The NBE solution was spin-coated onto the barrier film at 2000 r/min for 30 s without post-annealing. PVA solution was spin-coated onto the barrier film at 2000 r min^{-1} and thermally annealed at 120 °C for 20 min. The silver nanowire (AgNWs) solution was prepared according to the previous work,[68] which was spin-coated twice on the modified layer at a speed of 2000 r min^{-1} for 30 s and annealed at 120 °C for 30 min. These processes were carried out under the condition of avoiding the illumination of white light.

Fabrication of Organic Solar Cell Devices: The 1 cm^2 FOSCs were fabricated with an inverted structure of flexible electrode/ZnO/Active layer/MoO_3/Al. The ZnO electron-transporting layer was synthesized and dispersed in MeOH according to the previous work.[69] The C_{60} SAM solution in chloroform (0.2 mg mL^{-1}) was spin-coated onto the ZnO layer at 3000 r min^{-1} for 30 s, followed by thermal annealing at 110 °C for 10 min. The PM6 donor, L8-BO acceptor, and DIB solid additive were dissolved in chloroform at a weight ratio of 1:1.2:1 and stirred at 55 °C for 5 h. The active layer ink of PM6:L8-BO with a donor concentration of 7.5 mg mL^{-1} was deposited onto the C_{60} SAM layer at a speed of 2000 r min^{-1} for 30 s, and the active layer film was thermally annealed at 85 °C for 5 min. The PM6 donor, BTP-BO-4Cl, C-$PC_{61}BM$ acceptor, and DCBB solid additive were dissolved in chloroform at a weight ratio of 1:1.2:0.3:1.3 and stirred at 60 °C for 3 h. The active layer ink of PM6:BTP-BO-4Cl:C-$PC_{61}BM$ with a donor concentration of 7.5 mg mL was deposited onto the ZnO films at a speed of 2500 r min^{-1} for 30 s, and the active layer film was thermally annealed at 160 °C for 30 min. After annealing, the samples were transferred to the vacuum evaporation chamber. Finally, 10 nm MoO_3 layer and 200 nm Al layer were deposited onto the active layer under a vacuum level of less than 5×10^{-4} Pa. The devices with the structure of barrier film/NBE/AgNWs/ZnO/active layer/MoO_3/Al were irradiated for 5 min from AgNWs side using a white LED lamp (HSPY-60-05 LED curing lamp, 230 mW cm^{-2}).

Characteristics: XPS spectra of the barrier films were measured using a Thermo Scientific ESCALAB Xi^+ spectrometer with a monochromatic Al Kα X-ray source with an overall energy space of $\Delta E = 0.1$ eV. The transmittance spectra of the barrier film substrates and different electrodes were measured with the Lambda 750 UV-Vis-NIR spectrophotometer (PerkinElmer) under a standard measuring apparatus. The four-probe tester was used to test the sheet resistance of different electrodes. The bending and tearing test of electrodes was measured by recording the change in sheet resistance. The water contact angle of both the original barrier film and the modified surface was measured by a contact angle tester (SDC-350D). The surface morphology of flexible electrodes was measured by using a scanning electron microscope (Regulus8230). Current density-voltage (*J-V*) testing was performed in a nitrogen glove box using a solar simulator (100 mW cm^{-2}, XES-40S3) and a Keithley 2400 meter. The long-term storage stability of the unencapsulated and encapsulated devices was measured through testing the *J–V* curves after a period of storage in air with controlled temperature and humidity.

Supporting Information

Supporting Information is available from the Wiley Online Library or from the author.

Acknowledgements

This work was supported by the National Natural Science Foundation of China (22135001, 22475232), Suzhou Science and Technology Program (ST202219), "Dual Carbon" Science and Technology Innovation of Jiangsu Province (Industrial Prospect and Key Technology Research program) (BE2022021), Vanguard-Leading Goose+X R&D Project (2024C01090), Vacuum Interconnected Nanotech Workstation, Suzhou Institute of Nano Tech and Nano Bionics, Chinese Academy of Sciences (CAS) and Suzhou Science and Technology Program (ST202219).

Conflict of Interest

The authors declare no conflict of interest.

Author Contributions

Q.L. conceived the project. Y.C. conducted experiments and data analysis. C.Y. and W.S.L. provided the C-PCBM materials. W.X. performed the FT-IR, AFM, bending, shelf, and UV stability of the flexible electrodes. Y.H. characterized the devices. H.X. and K.S. synthesized the NBE materials. S.T.Y. fabricated the flexible electrodes. L.P.Z. measured the SEM images. Z.Y.L. and Y.B.Z. measured the XPS spectra. Y.C. contributed to the manuscript preparation. C.-Q.M. and Q.L. revised the manuscript. All the authors discussed the results and commented on the manuscript. Y.C., C.Y., and W.X. contributed equally to this work.

Data Availability Statement

The data that support the findings of this study are available in the supplementary material of this article.

Keywords

AgNWs, barrier film, flexible organic solar cells, hydrophilic-to-hydrophobic conversion, stability

Received: June 9, 2025
Revised: August 25, 2025
Published online:

---

[1] Z. Chen, J. Ge, W. Song, X. Tong, H. Liu, X. Yu, J. Li, J. Shi, L. Xie, C. Han, Q. Liu, Z. Ge, *Adv. Mater.* **2024**, *36*, 2406690.
[2] J. Xia, J. Zhu, H. Chen, G. Zeng, J. Wan, B. Zhang, S. Lee, J. Xu, J. Cao, X. Wu, J. Ding, L. Yang, W. Chen, C. Yang, Y. Li, Y. Li, *Angew. Chem., Int. Ed.* **2025**, 202501270.
[3] Z. Xiao, J. Liu, X. Chen, Z. Suo, X. Cao, N. Xu, Z. Yao, C. Li, X. Wan, Y. Chen, *J. Mater. Chem. A* **2025**, *13*, 2301.
[4] H. Lee, S. Jeong, J.-H. Kim, Y.-R. Jo, H. J. Eun, B. Park, S. C. Yoon, J. H. Kim, S.-H. Lee, S. Park, *npj Flex. Electron.* **2023**, *7*, 27.
[5] Y. Wang, Q. Chen, G. Zhang, C. Xiao, Y. Wei, W. Li, *ACS Appl. Mater. Interfaces* **2022**, *14*, 5699.
[6] D. Zhang, Y. Ji, Y. Cheng, X. Liu, Z. Xia, X. Liu, X. Liu, X. Yang, W. Huang, *J. Mater. Chem. A* **2024**, *12*, 15099.
[7] J. Wan, R. Wen, Y. Xia, M. Dai, H. Huang, L. Xue, Z. Zhang, J. Fang, K. N. Hui, X. Fan, *J. Mater. Chem. A* **2021**, *9*, 5425.
[8] S. Yang, X. Chen, Y. Pan, J. Fang, Y. Han, Z. Wang, F. Qian, W. Qi, K. Shui, Q. Zhang, F. Guo, Y. Sun, C. Q. Ma, Q. Luo, *Adv. Mater.* **2025**, *37*, 2500115.
[9] Z. G. Wang, J. B. Guo, Y. Q. Pan, J. Fang, C. Gong, L. X. Mo, Q. Luo, J. Lin, C. Q. Ma, *Energy Environ. Mater.* **2024**, *7*, 12592.
[10] Z. Xu, G. Xu, Q. Luo, Y. Han, Y. Tang, Y. Miao, Y. Li, J. Qin, J. Guo, W. Zha, C. Gong, K. Lu, J. Zhang, Z. Wei, R. Cai, Y. Yang, Z. Li, C. Q. Ma, *Natl. Sci. Rev.* **2023**, *10*, 285.
[11] Y. Han, Z. Hu, W. Zha, X. Chen, L. Yin, J. Guo, Z. Li, Q. Luo, W. Su, C. Q. Ma, *Adv. Mater.* **2022**, *34*, 2110276.
[12] X. Zheng, L. Zuo, K. Yan, S. Shan, T. Chen, G. Ding, B. Xu, X. Yang, J. Hou, M. Shi, H. Chen, *Energy Environ. Sci.* **2023**, *16*, 2284.
[13] S. Xiong, K. Fukuda, S. Lee, K. Nakano, X. Dong, T. Yokota, K. Tajima, Y. Zhou, T. Someya, *Adv. Sci.* **2022**, *9*, 2105288.
[14] Y.-C. Huang, C.-C. Lee, Y.-Y. Lee, S. Chung, H.-C. Lin, U. Kasimayan, C.-F. Li, S.-W. Liu, *Mater. Adv.* **2024**, *5*, 2411.
[15] N. Cui, Y. Song, C.-H. Tan, K. Zhang, X. Yang, S. Dong, B. Xie, F. Huang, *npj Flex. Electron.* **2021**, *5*, 31.
[16] H. Li, C. Zhang, J. Wei, K. Huang, X. Guo, Y. Yang, S. So, Q. Luo, C.-Q. Ma, J. Yang, *Flex. Print. Electron.* **2019**, *4*, 044007.
[17] Y. C. Huang, H. C. Cha, S. H. Huang, C. F. Li, S. R. M. Santiago, C. S. Tsao, *Polymers* **2023**, *15*, 4005.
[18] B. H. S. Miranda, L. d. Q. Corrêa, G. A. Soares, J. L. Martins, P. L. Lopes, M. L. Vilela, J. F. Rodrigues, T. G. Cunha, R. d. Q. Vilaça, S. Castro-Hermosa, L. Wouk, D. Bagnis, *Sol. Energy* **2021**, *220*, 343.
[19] R. Gong, Q. Yan, Z. Xing, H. Wang, L. Tan, X. Meng, X. Hu, Y. Chen, *Adv. Mater.* **2025**, *37*, 2501033.
[20] M. Wu, B. Ma, S. Li, J. Han, W. Zhao, *Adv. Funct. Mater.* **2023**, *33*, 2305445.
[21] H. Cao, W. He, Y. Mao, X. Lin, K. Ishikawa, J. H. Dickerson, W. P. Hess, *J. Power Sources* **2014**, *264*, 168.
[22] W. Song, Q. Ye, S. Yang, L. Xie, Y. Meng, Z. Chen, Q. Gu, D. Yang, J. Shi, Z. Ge, *Angew. Chem., Int. Ed.* **2023**, *62*, 202310034.
[23] J. Zhu, J. Xia, Y. Li, Y. Li, *ACS Appl. Mater. Interfaces* **2025**, *17*, 5595.
[24] C. P. Thompson, S. Hegedus, P. Carcia, R. S. McLean, *IEEE J. Photovolt* **2013**, *3*, 494.
[25] S. Castro-Hermosa, M. Top, J. Dagar, J. Fahlteich, T. M. Brown, *Adv. Electron. Mater.* **2019**, *5*, 1800978.
[26] S. Xiong, K. Fukuda, K. Nakano, S. Lee, Y. Sumi, M. Takakuwa, D. Inoue, D. Hashizume, B. Du, T. Yokota, Y. Zhou, K. Tajima, T. Someya, *Nat. Commun.* **2024**, *15*, 681.

[27] A. Maeda, R. Liu, K. Yu, S. Lee, K. Nakano, M. Takakuwa, S. Zhang, K. Tajima, K. Fukuda, S. Umezu, T. Someya, *JPhys Mater.* **2021**, *4*, 044016.

[28] H. Liu, D. Yuan, H. Jiang, S. Li, L. Zhang, J. Chen, *Energy Environ. Sci.* **2023**, *16*, 3474.

[29] M.-R. Zamani-Meymian, S. Sheikholeslami, M. Fallah, *Surfaces* **2020**, *3*, 319.

[30] N. Chen, P. Kovacik, R. M. Howden, X. Wang, S. Lee, K. K. Gleason, *Adv. Energy Mater.* **2014**, *5*, 1401442.

[31] C.-Y. Chang, K.-T. Lee, W.-K. Huang, H.-Y. Siao, Y.-C. Chang, *Chem. Mater.* **2015**, *27*, 5122.

[32] C. D. Petruczok, R. Yang, K. K. Gleason, *Macromolecules* **2013**, *46*, 1832.

[33] J. Ahmad, K. Bazaka, L. J. Anderson, R. D. White, M. V. Jacob, *Renew. Sust. Energ. Rev.* **2013**, *27*, 104.

[34] L. J. Sutherland, H. C. Weerasinghe, G. P. Simon, *Adv. Energy Mater.* **2021**, *11*, 2101383.

[35] Y. Zheng, L. Michalek, Q. Liu, Y. Wu, H. Kim, P. Sayavong, W. Yu, D. Zhong, C. Zhao, Z. Yu, J. A. Chiong, H. Gong, X. Ji, D. Liu, S. Zhang, N. Prine, Z. Zhang, W. Wang, J. B. Tok, Z. Bao, *Nat. Nanotechnol.* **2023**, *18*, 1175.

[36] E. N. Güler, A. Distler, R. Basu, C. J. Brabec, H.-J. Egelhaaf, *Flex. Print. Electron.* **2022**, *7*, 025003.

[37] H. C. Weerasinghe, N. Rolston, D. Vak, A. D. Scully, R. H. Dauskardt, *Sol. Energy Mater. Sol. Cells* **2016**, *152*, 133.

[38] H. Wang, Y. Pan, Y. Han, Z. Chen, T. Liu, L. Zhang, Q. Luo, C. Q. Ma, *Chin. J. Chem.* **2023**, *42*, 478.

[39] X. Chen, X. Wang, D. Fang, *Fuller. Nanotub. Carbon Nanostruct.* **2020**, *28*, 1048.

[40] K. Maria, L. Kozakova, T. Bakalar, J. Skvarla, *J. Anal. Chem.* **2020**, *75*, 1304.

[41] M. N. Masood, E. T. Carlen, A. van den Berg, *Appl. Surf. Sci.* **2015**, *337*, 105.

[42] Y. Uraoka, H. Yano, T. Hatayama, T. Fuyuki, *Jpn. J. Appl. Phys.* **2002**, *41*, 3637.

[43] E. Rossegger, D. Nees, S. Turisser, S. Radl, T. Griesser, S. Schlögl, *Polym. Chem.* **2020**, *11*, 3125.

[44] E. Rossegger, D. Hennen, T. Griesser, I. Roppolo, S. Schlögl, *Polym. Chem.* **2019**, *10*, 1882.

[45] K. Shui, Y. Fang, Z. Li, Z. Wang, S. Jiang, N. Yin, Q. Chen, F.-Q. Guo, J.-W. Zhao, J. Lin, C.-Q. Ma, *Flex. Print. Electron.* **2023**, *8*, 035019.

[46] J. Qin, N. Wu, W. Chen, B. Liu, Z. Wang, L. Zhang, N. Yin, Q. Chen, Z. B. Zhang, C. Q. Ma, *Small Methods* **2023**, *7*, 2300224.

[47] Z. Pan, M. Bora, R. Gee, R. H. Dauskardt, *Mater. Chem. Phys.* **2023**, *308*, 128289.

[48] Y. Ma, G. W. Sim, S. Jo, D. C. Hyun, J.-S. Roh, D. Ko, J. Kim, *Appl. Sci.* **2024**, *14*, 420.

[49] M. Gholami, F. Tajabadi, N. Taghavinia, A. Moshfegh, *Sci. Rep.* **2023**, *13*, 17511.

[50] N. M. Ainali, D. N. Bikiaris, D. A. Lambropoulou, *Polym. Degrad. Stab.* **2024**, *222*, 110692.

[51] S. Rostampour, R. Cook, S.-S. Jhang, Y. Li, C. Fan, L.-P. Sung, *Polymers* **2024**, *16*, 2249.

[52] X. Liu, Z. Zheng, J. Wang, Y. Wang, B. Xu, S. Zhang, J. Hou, *Adv. Mater.* **2021**, *34*, 2106453.

[53] Q. Liao, Q. Kang, Y. Yang, Z. Zheng, J. Qin, B. Xu, J. Hou, *CCS Chem.* **2022**, *4*, 938.

[54] H. Song, Y. Dong, Z. Zhang, J. Fang, C. Yue, Y. Yang, C. Liu, Q. Guo, H. Wang, Q. Luo, W.-S. Li, L. Yan, C.-Q. Ma, C. J. Brabec, *Chem. Eng. J.* **2025**, *503*, 158694.

[55] Y. Yang, J. Wang, Y. Zu, Q. Liao, S. Zhang, Z. Zheng, B. Xu, J. Hou, *Joule* **2023**, *7*, 545.

[56] J. Won Lim, C. Kyu Jin, K. Yong Lim, Y. Jae Lee, S.-R. Kim, B.-I. Choi, T. Whan Kim, D. Ha Kim, D. Kyung Hwang, W. Kook Choi, *Nano Energy* **2017**, *33*, 12.

[57] M. Song, J.-K. Kim, S.-Y. Yang, J.-W. Kang, *Thin Solid Films* **2014**, *573*, 14.

[58] M. Song, J. H. Park, C. S. Kim, D.-H. Kim, Y.-C. Kang, S.-H. Jin, W.-Y. Jin, J.-W. Kang, *Nano Res.* **2014**, *7*, 1370.

[59] D. Chen, C. Zhang, W. Wei, Z. Wang, T. Heng, S. Tang, G. Han, J. Zhang, Y. Hao, *Phys. Status Solidi A* **2015**, *212*, 2262.

[60] X. Xu, K. Fukuda, A. Karki, S. Park, H. Kimura, H. Jinno, N. Watanabe, S. Yamamoto, S. Shimomura, D. Kitazawa, T. Yokota, S. Umezu, T. Q. Nguyen, T. Someya, *Proc. Natl. Acad. Sci. U.S.A.* **2018**, *115*, 4589.

[61] S. Wang, S. Wu, Z. Ling, H. Chen, H. Lian, X. Portier, F. Gourbilleau, T. Marszalek, F. Zhu, B. Wei, T. Xu, *Org. Electron.* **2020**, *78*, 105593.

[62] Y. Li, R. Wen, P. Li, X. Fan, *ACS Appl. Energy Mater.* **2022**, *5*, 7692.

[63] W. Xing, Y. Chen, X. Wang, L. Lv, X. Ouyang, Z. Ge, H. Huang, *ACS Appl. Mater. Interfaces* **2016**, *8*, 26916.

[64] S. Lee, J. Kong, K. Lee, *Adv. Energy Mater.* **2016**, *6*, 1600970.

[65] Y. Ge, L. Hu, L. Zhang, Q. Fu, G. Xu, Z. Xing, L. Huang, W. Zhou, Y. Chen, *ACS Appl. Mater. Interfaces* **2020**, *12*, 10706.

[66] T. L. H. Mai, Z. Sun, S. Kim, S. Jeong, S. Lee, J. Park, C. Yang, *Energy Environ. Sci.* **2024**, *17*, 7435.

[67] J.-L. Wang, X.-Q. Chen, X. Yao, S.-C. Wu, L.-N. Liu, W.-J. Xiao, H. Wang, J. Li, Z. Lu, W.-S. Li, *Tetrahedron Lett.* **2017**, *58*, 2695.

[68] Z. Wang, Y. Han, L. Yan, C. Gong, J. Kang, H. Zhang, X. Sun, L. Zhang, J. Lin, Q. Luo, C.-Q. Ma, *Adv. Funct. Mater.* **2020**, *31*, 2007276.

[69] J. Guo, Y. Han, Z. Xu, W. Zha, J. Fang, Q. Luo, L. Liu, C.-Q. Ma, *Flex. Print. Electron.* **2022**, *7*, 025013.